



This is a repository copy of *Investigating the melt pool properties and thermal effects of multi-laser diode area melting*.

White Rose Research Online URL for this paper:
<https://eprints.whiterose.ac.uk/130126/>

Version: Published Version

Article:

Zavala-Arredondo, M., Ali, H., Groom, K.M. et al. (1 more author) (2018) Investigating the melt pool properties and thermal effects of multi-laser diode area melting. *International Journal of Advanced Manufacturing Technology*, 97 (1-4). pp. 1383-1396. ISSN 0268-3768

<https://doi.org/10.1007/s00170-018-2038-2>

Reuse

This article is distributed under the terms of the Creative Commons Attribution (CC BY) licence. This licence allows you to distribute, remix, tweak, and build upon the work, even commercially, as long as you credit the authors for the original work. More information and the full terms of the licence here:
<https://creativecommons.org/licenses/>

Takedown

If you consider content in White Rose Research Online to be in breach of UK law, please notify us by emailing eprints@whiterose.ac.uk including the URL of the record and the reason for the withdrawal request.



eprints@whiterose.ac.uk
<https://eprints.whiterose.ac.uk/>



Investigating the melt pool properties and thermal effects of multi-laser diode area melting

Miguel Zavala-Arredondo¹ · Haider Ali¹ · Kristian M. Groom² · Kamran Mumtaz¹ 

Received: 7 February 2018 / Accepted: 16 April 2018
© The Author(s) 2018

Abstract

Diode area melting (DAM) is a new additive manufacturing process that utilises customised architectural arrays of low-power laser diode emitters for high-speed parallel processing of metallic feedstock. The laser diodes operate at shorter laser wavelengths (808 nm) than conventional SLM fibre lasers (1064 nm) theoretically enabling more efficient energy absorption for specific materials. This investigation presents the first work investigating the melt pool properties and thermal effects of the multi-laser DAM process, modelling generated melt pools the unique thermal profiles created along a powder bed during processing. Using this approach process, optimisation can be improved by analysing this thermal temperature distribution, targeting processing conditions that induce full melting for variable powder layer thicknesses. In this work, the developed thermal model simulates the DAM processing of 316L stainless steel and is validated with experimental trials. The simulation indicates that multi-laser DAM methodology can reduce residual stress formation compared to the single point laser scanning methods used during selective laser melting.

Keywords Diode area melting · Additive manufacturing · Finite element · Cooling rate · Temperature gradient

Abbreviations

AM	Additive manufacturing
SLM	Selective laser melting
EBM	Electron beam melting
DAM	Diode area melting
FEM	Finite element model
TGM	Temperature gradient mechanism
CR	Cooling rate
DFLUX	Distributed heat flux
MPHF	Modified prismatic laser heat flux
LBP	Laser beam profile

1 Background

Additive manufacturing (AM) technologies are capable of creating geometrically efficient structures with low material wastage. Laser-based selective laser melting (SLM) and electron-based electron beam melting (EBM) AM systems are increasingly being used in high value sectors to directly manufacture metallic end-use parts from a variety of alloys. During processing, the melting source (deflected laser/electron beam) selectively scans and melts regions of a pre-deposited powder bed. Cross sections of the part are fused in layers, built up successively to create the complete 3D object. This method of layered fabrication, combined with the high precision of laser melting, allows for a greatly expanded design freedom with minimal feedstock waste.

Diode area melting (DAM) is a novel powder-bed-based AM process for the manufacture of metallic components with ability to process materials with melt temperatures in excess of 1400 °C [1] using a multi-spot array of low powered laser beams. The DAM heat input mechanism can improve SLM limitations with regard to process thermal evolution, which are known to induce high residual stresses and promote cracking due to the very high cooling rates involved. The thermal

✉ Kamran Mumtaz
k.mumtaz@sheffield.ac.uk

¹ Department of Mechanical Engineering, University of Sheffield, Sheffield S1 3JD, UK

² Department of Electronic & Electrical Engineering, University of Sheffield, Sheffield S1 3JD, UK

behaviour of DAM is analysed in the present work and compared to that of SLM reported in literature.

1.1 State-of-the-art in diode area melting

The DAM methodology replaces the traditional galvo scanning methodology used within single fibre laser SLM systems with multiple non-deflected low power laser diode beams that scan and selectively melt powdered feedstock material in parallel. A multi-layer $4.5 \times 4.5 \times 6$ mm stainless steel sample composed of multiple ~ 150 μm layers with areas of cross-sectional micro density comparable to SLM has been reported in [1]. The total laser power and scanning speed used for manufacturing the DAM 3D part were 50 W and 0.5 mm s^{-1} , respectively. Lack of fusion was observed in regions between layers as well as limited substrate bonding. An energy density 86 J mm^{-3} in DAM has been theorised as the minimum required for producing high-density parts with penetration depths similar to SLM [2]. In the present work, a finite element model (FEM) capable of simulating the DAM process is used for analysing the cooling rate and temperature gradient mechanisms that describe the DAM thermal evolution. The model was able to predict melt-pool dimensions within 91–94% accuracy. FEM-assisted parameter optimisation was used to compare the DAM thermal evolution with that of SLM for the same material. The FEM predicted DAM cooling rate and temperature gradient similar to those of optimised SLM methodologies with lower residual stress formation.

1.2 Residual stresses in selective laser melting (SLM)

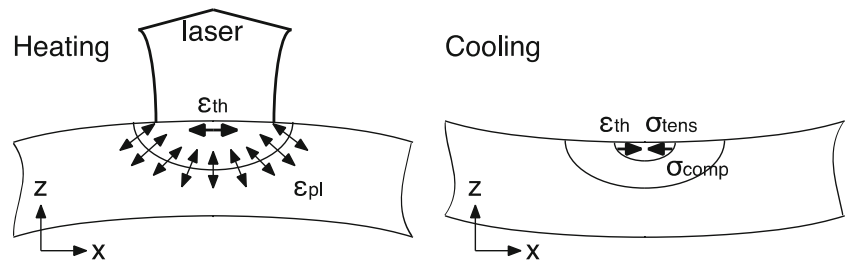
The rapid melting and solidification mechanisms during SLM lead to very high-temperature gradients that result in high residual stress formation [3]. The nature and origins of residual stresses in laser processes such as SLM are described in [4]. These can be either mechanical, thermal or plastic and can be typified by the dimensional scale that better describes the property under consideration. Three types of residual stresses are characterised in [4], denominated as Types I, II and III. Typically, Type I residual stress scale is used to characterise the SLM mechanism since it varies over large distances similar to the dimensions of the additively manufactured part. Residual stresses in SLM are unwanted since they can reduce the tolerance of the as-built part to an external applied force and cause part deformation when removed from the substrate. Moreover, residual stresses can reduce the strength of the part and promote the propagation of cracks from the surface. Laser-based processes are known to result in high levels of residual stresses due to the large thermal gradients inherent to the rapid melting-solidification mechanism. In [5], the temperature gradient mechanism (TGM) is described which causes residual stresses in sheet metal plates during laser heating and cooling phases as illustrated in Fig. 1. High-temperature gradients

develop due to the rapid heating of the upper sheet surface and the comparatively slow heat conduction through the lower surface. The laser-heated surface experiences a thermal expansion which is restricted by the underlying solid material inducing elastic compressive strains. The laser-heated surface is plastically compressed when the material's yield strength is reached causing in turn bending away from the laser beam. A counter bending occurs during the cooling phase due to the thermal contraction of the cooling surface. In SLM, the bending and counter bending mechanisms are inhibited by the underlying solid material (i.e. solid substrate and/or previously solidified layers). During the cool-down phase, shrinkage of the thermally contracted top layers is inhibited resulting in tensile stresses in the added top layer and compressive stress below. In [5], it was concluded that it is possible to reduce residual stresses by (1) applying heat treatment using the laser source and/or (2) reducing temperature gradients by heating the substrate plate.

1.3 Temperature gradients and cooling rate in selective laser melting (SLM)

The temperature gradients and cooling rate along the x , y and z -directions during SLM of stainless steel have been modelled in [6]. The model was validated with experimental tests. Figure 2 shows the cooling rate of five scan tracks in (a) the x - y plane at top surface of the powder bed and (b) the y - z plane along the cross-section (A-A') at the centre of the processing region of a typical SLM scanning strategy. Figure 2c, d shows the thermal history of Point A3, in Fig. 2a, and the temperature distribution in the z -direction, respectively. The process parameters used in Fig. 2a–d are laser power 120 W, laser diameter $140 \mu\text{m}$, hatch spacing $65 \mu\text{m}$, layer thickness $50 \mu\text{m}$ and scanning speed 715 mm s^{-1} . It can be seen in Fig. 2a that cooling rates tend to be higher at the lateral regions of the processing area, along the scanning direction (i.e. both at the beginning and ending of individual scanning vectors). Higher cooling rates along the scanning vectors can be due to the presence of un-melted (cold) material at the vicinity of the adjacent regions. Lower cooling rates can be seen at the centre of the processing area, perpendicular to the scanning direction. Such regions are surrounded by previously melted and solidified (hot) material which may induce lower solidification rates. The ratio s/d (solidification distance / beam diameter) can be used to explain the temperature gradients along and across the scanning direction. The ratio describes the temperature gradient proportion, where a higher s/d ratio describes higher temperature gradients. Typical SLM s/d values describing elongated-tail-shaped temperature distributions (i.e. along the scanning direction) can reach $s/d = 2.2$ (i.e. $220 \mu\text{m}$ solidification distance/ $100 \mu\text{m}$ beam diameter reported in simulations conducted in [7]). The typical SLM temperature distribution of an elongated-tail shape suggests a much lower s/d ratio in directions perpendicular to the scanning vector [8].

Fig. 1 Temperature gradient mechanism inducing residual stress in metallic sheet plates. Adapted from [5]



This explains the higher temperature gradients along the scanning direction compared to those perpendicular as reported in [6]. Cooling rates can be observed to reduce steeply along the cross section A-A' during tracks 1 and 2, reaching stable levels in Points A3 to A5, in Fig. 2a. Starting from track 3, an invariance in the cooling rates across laser tracks is shown, which is also depicted in Fig. 2b by a constant melt depth after track 3. The melt depth and cooling rate invariance are expected to continue if more tracks are analysed. The thermal history of point A3 is plotted in Fig. 2c. Here, several temperature peaks are observed due to accumulation of subsequent laser tracks. Two lower secondary peaks (first and last in Fig. 2c) can reach melting temperatures before and after the main melting peak respectively, inducing localised laser heat treatment. The cooling rate can be obtained from Eq. 1,

$$\text{Cooling rate } (^\circ\text{C s}^{-1}) = \frac{\Delta T}{\Delta t} = \frac{|T_{\text{liquidus}}(^\circ\text{C}) - T_{\text{solidus}}(^\circ\text{C})|}{|t_{\text{liquidus}}(\text{s}) - t_{\text{solidus}}(\text{s})|} \quad (1)$$

where $T_{\text{liquidus}} = 1425 \text{ }^\circ\text{C}$ and $T_{\text{solidus}} = 1385 \text{ }^\circ\text{C}$ for stainless steel [9]. The cooling rates of the three temperature peaks observed in Fig. 2c are $2.08\text{E} + 05 \text{ } (^\circ\text{C s}^{-1})$, $1.07\text{E} + 05 \text{ } (^\circ\text{C s}^{-1})$ and $1.51\text{E} + 05 \text{ } (^\circ\text{C s}^{-1})$ for the first, main and last peak, respectively. In Fig. 2d, the slope of the temperature distribution curve in the z-direction becomes steeper as z increases, which is an indication of increasing temperature gradient and cooling rate when distance into the substrate (or previously solidified layers) is increased. The instant temperature gradient from the top surface of the substrate to the melt depth is $|\Delta T/\Delta z|_{\text{ (top surface to melt depth)}} = 11.16 \text{ }^\circ\text{C } \mu\text{m}^{-1}$.

A comparison of Fig. 2a, b shows that cooling rates tend to be higher at the intersection with the substrate (Fig. 2b) than at the top surface of the process layer (Fig. 2a). This is in agreement with the study conducted in [10] who evaluated the residual stress distribution of a stainless steel sample along the z-direction. Figure 3 shows the residual stresses curve profile for central regions of a $3 \times 3 \text{ cm}$ SLM one-layer samples.

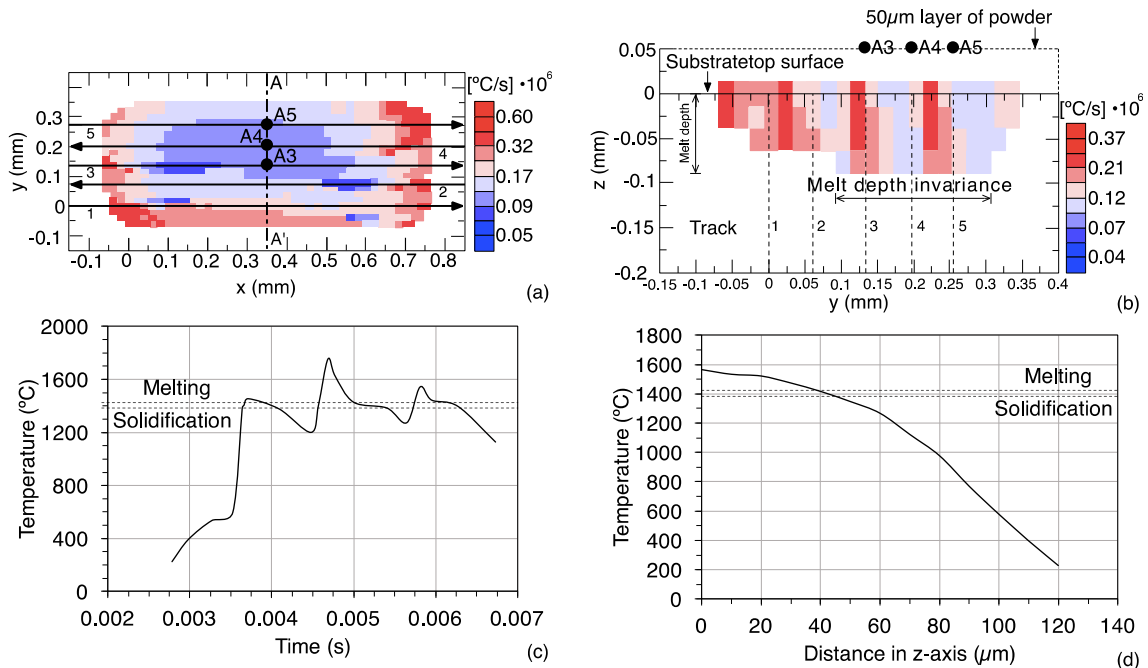


Fig. 2 Cooling rate in the **a** x-y plane at the top surface of the powder bed and **b** y-z plane along the cross section A-A'. **c** Thermal history of point A3 and **b** instant temperature distribution in z-direction for laser power

120 W, hatch spacing 65 μm , layer thickness 50 μm and scan speed 715 mm s^{-1} . Adapted from [6]

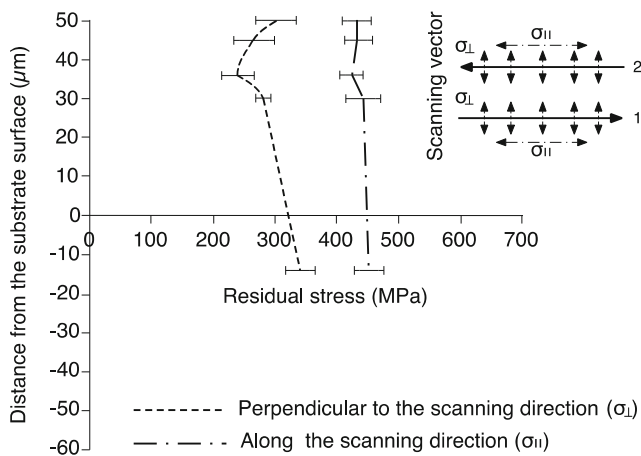


Fig. 3 Residual stress curve profile for central regions of a 3×3 cm one-layer sample. Adapted from [10]

The parameters used in Fig. 3 were laser power 50 W, laser diameter $70 \mu\text{m}$, hatch spacing $60 \mu\text{m}$, layer thickness $50 \mu\text{m}$ and scanning speed 100 mm s^{-1} . Figure 3 shows that residual stresses tend to be higher in regions closer to the substrate surface. Also, Fig. 3 shows higher levels of residual stresses along the scanning direction than those perpendicular to the scanning vectors. It can be concluded that cooling rates and residual stresses are directly correlated as the distribution of the highest cooling rates shown in Fig. 2a, b are represented by the highest levels of residual stresses in Fig. 3.

The microstructure of the material can be an indication of the mechanical properties of the part. For instance, hardness can increase if grain size is reduced. Fine microstructures are typical of laser-based processes due to their characteristic rapid cooling. Rapid solidification processes such as SLM can have cooling rates ranging from 10^3 to 10^7 [11]. The higher the cooling rate, the higher the material hardness. However, too high cooling rates may promote cracking in brittle materials. The primary dendrite arm spacing λ of stainless steel components can be used to characterise grain size as described in Eq. 2.

$$\lambda_1(\mu\text{m}) = 80(\text{CR})^{-0.33} \quad (2)$$

where CR refers to the cooling rate in K s^{-1} or $^\circ\text{C s}^{-1}$. The relation of primary dendrite arm spacing λ_1 with grain size is defined in [6]. Typical cooling rates in SLM of stainless steel

can be on the order of magnitude $\sim 10^5$ to $\sim 10^6$ $^\circ\text{C s}^{-1}$ as reported in [6], which result in cell spacing ranging from $\lambda_1 = \sim 0.84\text{--}1.79 \mu\text{m}$. Such values are characteristic of very fine microstructures typical of extremely hard components that can be susceptible to cracking.

1.4 Mechanisms for reducing residual stress build-up

In Sect. 1.2, the mechanisms for reducing residual stress build-up have been presented, namely (1) applying heat treatment using the laser source and (2) heating the substrate plate. These mechanisms are typically used for reducing thermal gradients and cooling rates in SLM. In [6] (see Sect. 1.3) it is shown that processing with $\sim 50\%$ scan-tracks overlap (hatch spacing $<$ laser diameter) can induce up to three temperature peaks above the melting point of the process material which might result in selective re-melting of regions exhibiting cooling rate invariance (see Fig. 2a, b). A similar behaviour was observed when using hatch spacing equal to laser diameter in [12]. However, when processing with hatch spacing $>$ laser diameter, no selective re-melting occurred. Selective re-melting can be scaled-up to the whole bed by using re-scanning strategies (i.e. re-melting by scanning the process layer multiple times). Re-scanning strategies together with substrate pre-heating were used in [13] to produce high-density stainless steel SLM parts by reducing thermal gradients and cooling rates. They observed a strong influence of these parameters on the properties of the as-built part. It was observed that the highest pre-heating temperature tested (200°C) + re-scanning resulted in samples with lower surface roughness and higher density. However, re-scanning by itself (i.e. without the assistance of substrate pre-heating) induced more cracks due to the formation of brittle martensite phase promoted by the higher cooling rates. Re-melting every layer can thus induce very high residual stress build-up and lead to cracking. It was concluded that lowering the thermal gradients and cooling rates by pre-heating the substrate can promote less martensite formation which can in turn reduce the thermal stresses and the amount of cracking. Moreover, in [14], it was reported that higher pre-heating temperatures can completely alleviate residual stresses by effectively minimising cooling rates and temperature gradients.

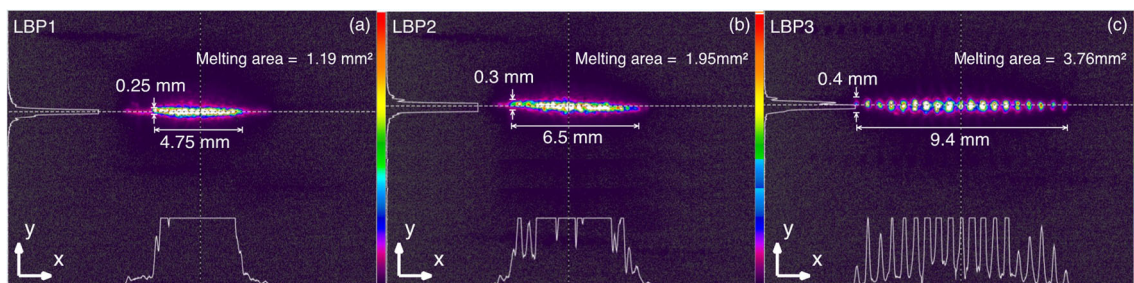
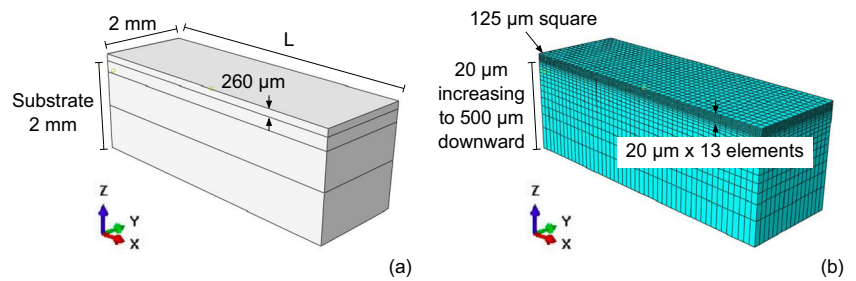


Fig. 4 Laser beam profiles dimensions and total melting areas. **a** LBP1. **b** LBP2. **c** LBP3. Adapted from [2]

Fig. 5 **a** Model and **b** mesh dimensions. Dimension L varies from $L = 6$ mm for LBP1 to $L = 10$ mm for both LBP2 and LBP3



1.5 Melt-pool penetration into substrate

In SLM, penetration of the melt-pool into the substrate allows for deposition of further layers without removing the previously melted layer, while the wiper moves along the substrate. A density analysis for SLM processing of 316L stainless steel was performed in [15] in order to identify the optimum process parameters for achieving > 99% part's density. A range of laser powers (250–400 W) and scan speeds (1500–1900 mm s⁻¹) were investigated, resulting in substrate penetration depths ranging from ~ 65 to ~105 μm. Such penetration depths allow re-melting of previously processed layers (n.b. typical layer thickness in SLM can be 50 μm) which facilitates the formation of an even surface. When the surface is even, the powder distribution of the next layer will be more homogenous and will reduce the entrapment of air [16]. This can reduce porosity and improve the density of the part. Such penetration depths are therefore a requirement for high density in DAM components.

2 Modelling the diode area melting process

An isotropic enhanced thermal conductivity model has been adapted from the model developed in [7] to simulate DAM processing of 316L stainless steel powder. The model takes into account the DAM Laser Beam Profiles (LBPs) and process parameters (i.e. laser power and scan speed) presented in the DAM experimental investigation conducted in [2]. The non-linearity of temperature-dependant material properties and phase changes is also considered. The modelling approach used in the present work is based upon the concept of a moving volumetric heat source (typically used in SLM modelling [17]) with enhanced penetration

Table 1 Thermal properties of process 316L stainless steel powder and mild steel substrate [9]

Material	Latent heat (mJ t ⁻¹)	Solidus temperature (°C)	Liquidus temperature (°C)
316L SS powder	2.85E + 11	1385	1425
Mild steel substrate	2.72E + 11	1394	1538

depth, combined with enhanced thermal conductivity through the substrate and the surrounding powder to improve computational efficiency, as described in [7]. The aim of the present work is to simulate the DAM process using optimised conditions that enable process energy density of 86 J mm⁻³, which has been theorised as the minimum required for processing fully dense multi-layer parts in the densification analysis conducted in [2]. The cooling rates, thermal distribution and temperature gradients of DAM are contrasted with those of SLM in order to compare the two different heat input mechanisms.

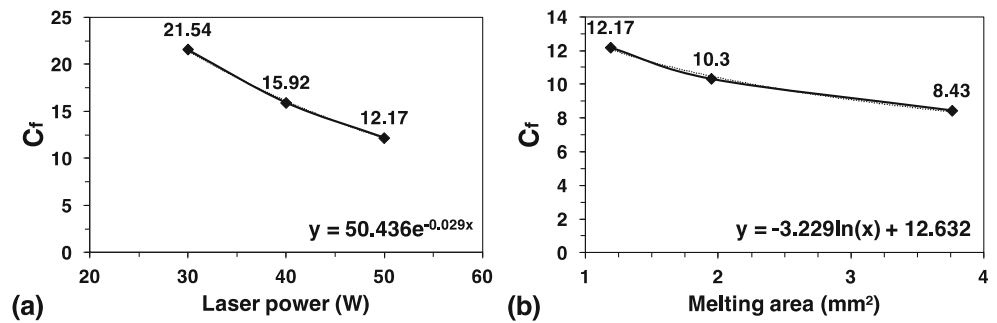
2.1 Laser heat source modelling

An ABAQUS DFLUX (Distributed Heat Flux) subroutine written in FORTRAN was used to simulate the laser as a moving volumetric heat source. This approach was used to account for the laser penetration effect into the powder, which according to [18] is 120 μm for stainless steel 316L powder. To make the simulation more efficient, the volumetric heat source was applied to a 260 μm-thick layer of powder, as used in the DAM densification analysis conducted in [2], along with a 250 μm depth into the substrate [7]. A Modified Prismatic laser Heat Flux (MPHF) model, similar to the cylindrical representation model explained in [19, 20], was used in the present work to represent the variation of radial laser intensity. Equation 3 shows the MPHF model, describing the heat flux of the rectangular multi-beam laser output typical of the DAM process,

$$q_{\text{mod prism}} (\text{Wmm}^{-2}) = \frac{0.864\alpha P}{b \times h} \quad (3)$$

where P is the laser power in W, and b and h are the base and height of the rectangular-shaped multi-beam laser diode irradiation on the powder bed top surface. From the DAM laser beam profiles (LBPs) described in [2], these are $b = 4.75$ mm and $h = 0.25$ mm for LBP1, $b = 6.5$ mm and $h = 0.3$ mm for LBP2 and $b = 9.4$ mm and $h = 0.4$ mm for LBP3 (Fig. 4). α is the laser absorptivity value for the 316L stainless steel powder bed. An absorption coefficient $\alpha = 0.5$ was used for the present work as used in [2]. The LBPs shown in Fig. 4 are top powder-bed views obtained

Fig. 6 Factor c_f for varying **a** laser power and **b** total melting/beam area (i.e. varying LBPs). Melting/beam area in **a** was 1.19 mm^2 (LBP1), and a range of scanning velocities was used (i.e. 1, 3 and 5 mm s^{-1}). Laser power and scan speed in **b** were fixed to 50 W and 5 mm s^{-1} , respectively



using a Spiricon camera-based beam profiler, and an opal glass target as described in [1] and the beam dimensions were measured using Ophir BeamMic software. It can be seen that the power distribution tends to be flatter whilst reducing beam dimensions (i.e. reducing individual spot size and spot period). LBP1 showed a typical flat-top laser profile with a homogeneous power distribution across the length of the profile. Equation 4 shows the laser intensity in the radial direction I_r (W mm^{-2}) used in the present model,

$$I_r (\text{Wmm}^{-2}) = c_f \cdot q_{\text{mod prism}} \tag{4}$$

where c_f is the correction factor required for achieving melt pool size and temperature distribution in good agreement with published results. c_f was calculated through FEM trials for different process parameters. The laser intensity in the melt depth direction, described by I_z (mm^{-1}), has been modelled as a parabolic relation as presented in [7]. Equation 5 shows the heat flux definition that describes the moving heat source simulation used in the present work,

$$\dot{q} (\text{Wmm}^{-3}) = (I_r \cdot I_z) \tag{5}$$

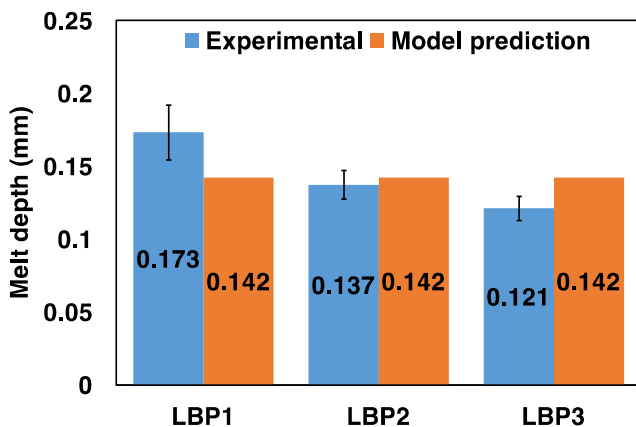


Fig. 7 Experimental and simulated melt depth dimensions for the different laser beam profiles LBP1–3. Laser power and scan speed remained constant at 50 W and 5 mm s^{-1} , respectively. Each LBP was simulated using the corresponding c_f from Fig. 6b where LBP1, 2 and 3 corresponds to 1.19 , 1.95 and 3.76 mm^2 , respectively

2.2 Simulation model

A simulation model consisting of a single $260 \text{ }\mu\text{m}$ layer of 316L stainless steel powder deposited upon a 2 mm thick mild steel substrate is presented in this work. The dimensions of the simulated substrate vary with the different LBPs modelled and range from $6 \times 2 \times 2 \text{ mm}$ for LBP1 simulation to $10 \times 2 \times 2 \text{ mm}$ for both LBP2 and LBP3 simulation (Fig. 5a). A 1.2 mm -length track (moving along the y -direction) was observed to result in a penetration depth invariance as described in Sect. 1.3, Fig. 2b. The solidification behaviour and cooling rate are expected to remain constant if a longer track is analysed. Therefore, a 1.2 mm scan was used to simulate the DAM process. Numerical simulation is carried out using the ABAQUS finite element package. Mesh element type DC3D8 (i.e. 8-node linear heat transfer brick element) was used. Figure 5b shows the $125 \times 125 \times 20 \text{ }\mu\text{m}$ mesh size used for the powder layer. The layer is composed of 13 elements in the z -direction to create the $260 \text{ }\mu\text{m}$ layer thickness. The substrate mesh was biased to move from $20 \text{ }\mu\text{m}$ at the top, increasing to $500 \text{ }\mu\text{m}$ at the bottom in order to keep the number of mesh elements to a minimum and reduce the model size and compilation time. The initial temperature of the substrate is $25 \text{ }^\circ\text{C}$. The rectangular heat source dimensions on the top surface of the powder bed vary with respect to the different beam profile dimensions (i.e. LBP1, LBP2 and LBP3), as described in Sect. 2.1. The nodal temperatures are monitored in time steps to determine material phase changes. The material properties are updated for the appropriate elements/nodes (interpolating when necessary) as the laser moves continuously along the simulated region (i.e. scanned track) until the whole defined geometry has been analysed. The material properties used in the model are summarised in Table 1. Temperature-dependent properties are detailed in [21].

2.3 Correction factor for varying parameters

To simulate the DAM melting process, multiple FE iterations were undertaken in order to identify the appropriate correction factor c_f described in Sect. 2.1, for the different process

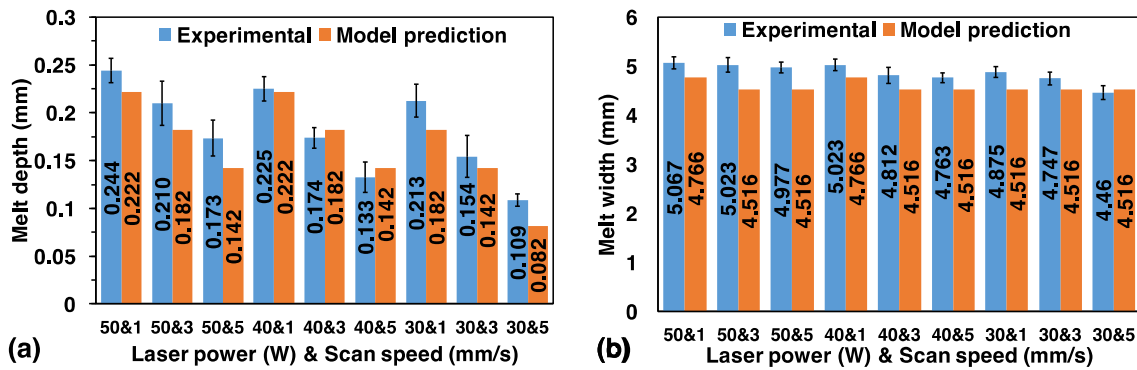


Fig. 8 Experimental and simulated **a** melt-depth and **b** melt-width dimensions for LBP1, varying laser power and scan speed. Each combination of parameters was simulated using the corresponding c_f from Fig. 6a for the different laser powers

parameters (i.e. laser power, scan speed and melting area). The iterations were conducted until the modelled melt dimensions approached the geometrical data experimentally acquired in literature, to the minimum % error possible. Therefore, c_f has to be considered as a boundary condition in the present DAM FEM. It was observed that laser power and beam dimension (i.e. melting area of a given LBP) were the only parameters defining c_f . Scan speed was observed to have a negligible effect in determining c_f . Therefore, c_f remained constant at varying scan speeds for a given laser power and LBP. Figure 6a plots the chosen c_f for varying laser power (i.e. 30, 40 and 50 W) and scanning velocities (i.e. 1, 3 and 5 mm s⁻¹) at constant LBP1 with a melting area of 1.19 mm². Figure 6b plots the chosen c_f for varying melting area (i.e. 1.19, 1.95 and 3.76 mm² for LBP1, LBP2 and LBP3, respectively) at constant 50 W and 5 mm s⁻¹. Trend lines are fitted for both plots, allowing extraction of c_f for process optimisation (i.e. using higher laser power and smaller melting area). The equations shown in Fig. 6a, b that describe the effect of laser power and melting area, respectively, were used to extract c_f for the process optimisation model.

3 Model validation

In order to determine the suitability of the FEM for predicting temperature evolution in DAM of stainless steel 316L, a comparative study with the experimental work reported in [1] was conducted. The simulated melt-pool dimensions were compared with the experimental observations published in [2],

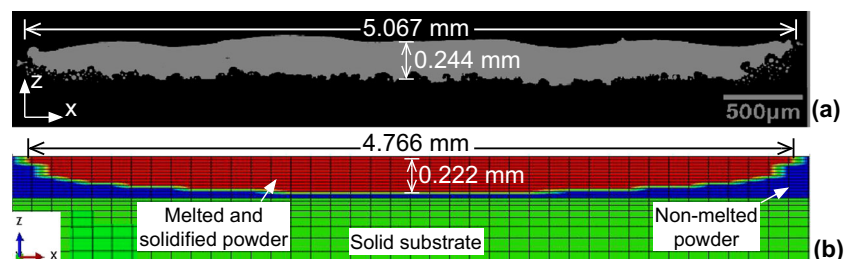
for a range of process parameters. The simulated temperature evolution was determined by measuring the nodal thermal history of defined points when irradiated by the moving laser heat source. The present section details the validation of the SLM model adapted for DAM simulation.

3.1 Melt-pool dimensions

In the present section, experimental melt-pool dimensions are compared with simulated values using the corresponding c_f described in Fig. 6. Figure 7 shows the measured and simulated melt depths for varying laser melting/beam areas (LBP1–3) at constant 50 W and 5 mm s⁻¹. It is assumed that the c_f trend as a function of melting area (see Fig. 6b) is the same at any constant power and speed. It was reported in [2] that LBP1 showed the more consistent results when varying energy density parameters (i.e. laser power and scan speed). Several failed samples were reported using lower energy density levels with LBP2 and 3. Therefore, only LBP1 were modelled for varying laser power and scan speed.

Figure 8 shows the measured and simulated melt dimensions for LBP1. Figure 8a compares the average experimental and simulated melt depths as a function of laser power and scan speed. Figure 8b shows a comparison of experimental melt widths against the simulated values for varying laser power and scan speed. Good agreement between experimental findings and simulated values of melt dimensions (i.e. melt depth and width) for varying parameters (i.e. laser power, scan speed and melting/beam area) was observed. Figure 9 shows an example of the experimentally measured melt dimensions

Fig. 9 **a** Experimentally measured melt dimensions for 316L stainless steel powder processed from 260 μ m layer thickness with 42 J mm⁻³ energy density. **b** Melt dimensions predicted by ABAQUS finite element thermal model



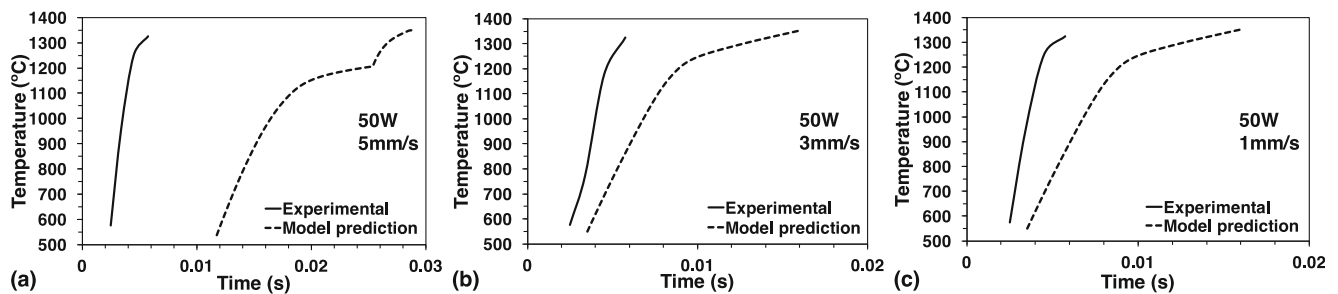


Fig. 10 Comparison of the simulated temperature rate in XY-plane with the experimentally measured during DAM processing of 316L stainless steel at 50 W and **a** 5, **b** 3 and **c** 1 mm s⁻¹

(Fig. 9a) together with the modelled melt dimensions (Fig. 9b) using the DAM process parameters (50 W power and 1 mm s⁻¹ scan speed) that resulted in the highest part density (99.68% cross-sectional micro density and 87.29% cross-sectional macro density) from the parametric investigation conducted in [2]. The experimentally acquired melt dimensions of 5.067×0.244 mm are in good agreement with the FEM simulated dimensions of 4.766×0.222 mm. The predicted melt-width is $\sim 6\%$ less than the average experimentally measured, and the predicted melt depth is 9% less than the average experimentally measured.

3.2 Thermal evolution and maximum temperature

The thermal history predicted by the FEM has been compared to the experimentally acquired temperature evolution in [1] (details of the equipment used, temporal and geometrical resolution, etc. used to record the experimentally acquired temperature fields can be found in [1]). The temperature transient was measured from the top surface of the powder bed (XY-plane) for a range of scan speeds with 50 W laser power across the irradiating laser stripe. Due to image saturation, the experimentally acquired temperature range was limited to a maximum measured temperature of 1350 °C. The nodal thermal history of a single central point across the beam spatial distribution is compared to the experimental data within the measured temperature range. Figure 10 shows this comparison for the three different scan speeds (5, 3 and 1 mm s⁻¹) investigated in [1]. It can be seen in Fig. 10a–c that temperature rises steeply up to ~ 1250 °C for all the scan speeds studied, before appearing to saturate to higher temperatures. Better agreement between simulated and experimental data is observed at slower scan speeds (i.e. higher energy density). However, no significant difference was observed when varying scan speed from 3 to 1 mm s⁻¹ both in the experimental and the modelled temperature evolution. From the FEM simulation, the maximum predicted temperatures for the different scanning speeds were 1510, 1519 and 1565 °C for 5, 3 and 1 mm s⁻¹, respectively. Figure 11 shows the maximum temperatures and the nodal thermal evolution predicted by the FEM for the different scan speeds investigated. Cooling rates were observed to

decrease significantly for slower scan speeds. Temperatures in excess of 1350 °C could not be experimentally measured. However, density analysis conducted in [1] indicated that melting was achieved, exceeding the melting temperature of stainless steel powder (1450 °C) without reaching too high temperatures that may have caused boiling. The results presented in Figs. 10 and 11 show that the thermal evolution, temperature trend and maximum temperatures predicted by the FEM agree well with the experimental data. It can be assumed that accurate predictions of the cooling rate and temperature gradients can be modelled, which might provide insight into the residual stress build-up.

4 Results and discussion

The present section describes the effect of layer thickness in DAM. Also presented is the process optimisation methodology, using the correction factor derived from equations in Figs. 6a, b. DAM modelling and simulation have been used to investigate the cooling rates and temperature gradients inherent to the process. Finally, the DAM optimised model is compared with SLM cooling rate, temperature gradient and penetration depth into substrate.

4.1 Effect of layer thickness

In order to investigate the effect of layer thickness, the model was adapted to model 200 and 150 μm layer thicknesses. For this, 10×20 μm elements and 8×18.75 μm elements in the z-axis (layer depth) were used to model 200 and 150 μm layer thickness, respectively. Figure 12 shows cross-sectional views of the temperature distribution for the 200 and 150 μm layer thicknesses modelled at 50 W laser power and 1 mm s⁻¹ scan speed. As described in Sect. 3.2, no significant difference in the process thermal evolution was observed when reducing scan speed below 3 mm s⁻¹. Therefore, it can be assumed that the scan speed 1 mm s⁻¹ modelled can be a good representation of the thermal history of 0.5 mm s⁻¹ scan speed reported in literature for the DAM 3D part (see Sect. 1.1). It can be seen in Fig. 12a that for a 200 μm layer thickness, temperatures in

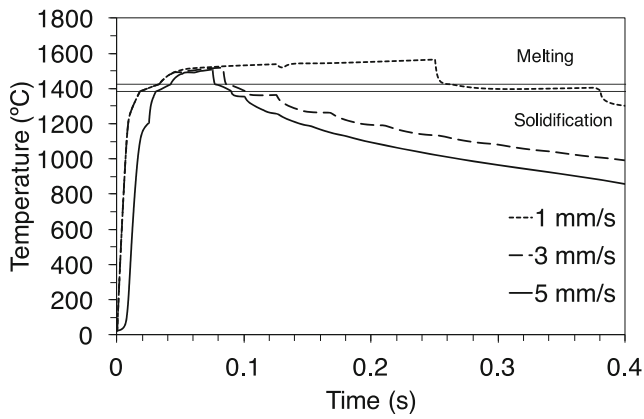


Fig. 11 Simulated nodal temperature transient for a range of scan speeds at 50 W and LBP1. Maximum simulated temperatures are 1510, 1519 and 1565 °C for 5, 3 and 1 mm s⁻¹, respectively

excess of the 316L stainless steel melting point (1450 °C) can be achieved uniformly across the scanning direction. In contrast, the melting temperature could not be reached when simulating the processing of 150 μm layer thickness (Fig. 12b). In this case, the laser-induced heat irradiated at the top surface of the powder bed rapidly dissipated into the solid substrate, which prevented reaching the melting point. When using 150 μm layer thickness, the high thermal conductivity of the solid substrate had a stronger influence on the temperature distribution. For the thicker 200 μm layer, lower thermal conductivity within the powder bed prevented such rapid heat-sinking into the substrate and better maintained the temperature distribution within the laser-irradiated bed, allowing temperatures in excess of 1450 °C to be reached. The aforementioned stainless steel DAM 3D part was processed at 50 W and 0.5 mm s⁻¹. However, a heat dissipation mechanism similar to that described here, and shown in Fig. 12b, may have prevented good inter-layer bonding in specific and random locations of non-uniform layer thickness.

Fig. 12 Cross-section images of the FEM showing temperature distribution for **a** 200 and **b** 150 μm layer thickness with LBP1, 50 W and 1 mm s⁻¹ (42 J mm⁻³ energy density)

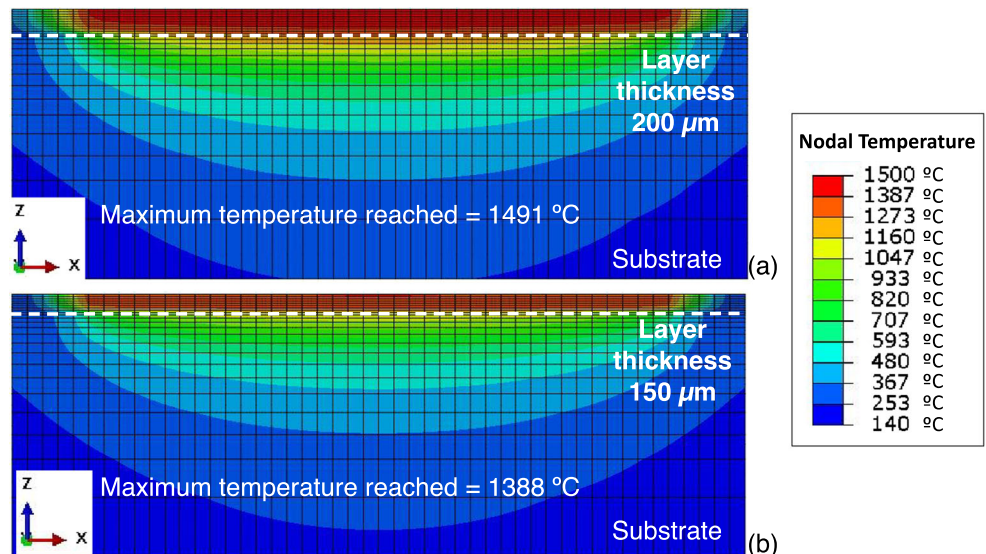


Table 2 Parameters used for DAM optimisation

Total laser power	100 W
Scan speed	6.12 mm s ⁻¹
Energy density	86 J mm ⁻³
Individual laser diameter	100 μm
Spot period (hatching space)	100 μm
Total melting/beam area	0.19 mm ²

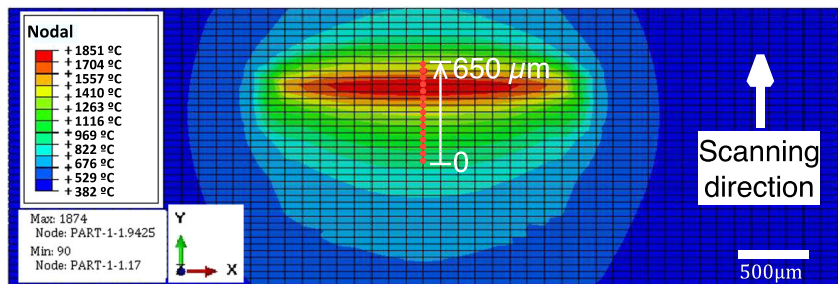
4.2 Process optimisation

A minimum energy density of 86 J mm⁻³ is suggested in literature for manufacturing high-density 3D DAM parts and achieving substrate bonding. Equation 6 shows that energy density is directly proportional to laser power and indirectly proportional to beam size and scan speed.

$$\text{Energy density} \left(\frac{\text{J}}{\text{mm}^3} \right) = \frac{\text{total laser power (W)}}{\text{total beam area (mm}^2) \times \text{scan speed} \left(\frac{\text{mm}}{\text{s}} \right)} \quad (6)$$

Therefore, higher energy densities can be attained by increasing laser power, reducing melting area and/or reducing the scan speed. The total processing time depends directly on scan speed; therefore, increasing scanning velocity is desirable for DAM optimisation, which in turn requires an increase in laser power and/or a decrease in melting area. An increase in total laser power can be achieved by multiplexing the output from multiple laser diode bars resulting in 100 W total laser power. Optimisation of the beam delivery system (by varying collimators and focusing lenses' focal length) can reduce the total melting/beam area by reducing individual beam

Fig. 13 Simulated temperature distribution at the top surface of the powder bed, along the scanning direction using optimised DAM configuration with 100 W and 6.12 mm s⁻¹. The red spots show the location of the 15 nodes/points along 700 μm in the scanning direction for nodal temperature measurement



dimensions and spots period. A DAM optical configuration composed by an array of multiple 100 μm diameter beams (i.e. typical laser dimension in SLM) has been modelled. The theoretically optimised optical configuration model accounts for the effect of × 19 individual melting spots, providing a total beam area $A = 1.9 \text{ mm} \times 0.1 \text{ mm} = 0.19 \text{ mm}^2$ considering scan spacing = individual spot diameter (as identified in Sect. 1.4 to be the minimum condition for selective remelting in SLM), with a flat-top laser intensity profile similar to that shown by LBP1 in Fig. 4a. The fit to the data shown in Fig. 6b describes the c_f trend in terms of total melting/beam area. For the optimised $A = 0.19 \text{ mm}^2$, a factor $c_f = 18.12$ has been calculated using this equation. A difference of 5.82 resulted from comparing the c_f of the optimised total melting/beam area (i.e. 0.19 mm^2) with that of LBP1 (i.e. 1.19 mm^2), as was used in the c_f trend analysis shown in Fig. 6a. The c_f trend for varying laser power is described by the equation describing the fit to the data in Fig. 6a. The c_f for the optimised model, increasing laser power to 100 W and using constant total melting/beam area $A = 0.19 \text{ mm}^2$, can be calculated using Eq. 7.

$$c_f = 50.436 \cdot \text{EXP}(-0.029 \cdot P) + 5.82 \tag{7}$$

where P is laser power in W, although c_f is dimensionless. Table 2 shows the parameters used in the optimised DAM model.

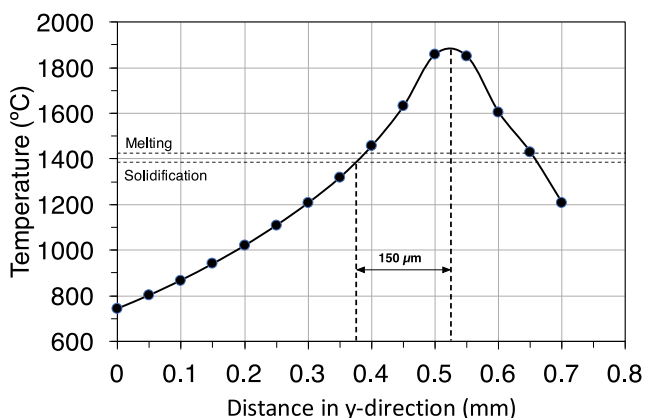


Fig. 14 Instant temperature distribution along the scanning direction. Each depicted data point represents a single red spot in Fig. 13

A 50 μm layer thickness, as is typical in SLM, was considered in the process optimisation model. To account for the optimised 100 μm single spot size and 50 μm layer thickness, the powder bed was adapted to $125 \times 50 \text{ μm}$ in the XY plane with $L = 6 \text{ mm}$ (see Fig. 5a) and $16.667 \text{ μm} \times 3$ elements in the z-direction.

4.3 Thermal spatial distribution

The modelled temperature distribution of the top surface of the powder bed along the scanning direction is shown in Fig. 13 for the DAM optimised configuration. The instant temperature of 15 nodes/points, 700 μm along the scanned track (as detailed in Fig. 13), has been extracted in order to plot the predicted thermal distribution along the scanning direction. Maximum temperature 1851 °C has been predicted (see nodal temperature label in Fig. 13). Figure 14 shows the extracted spatial thermal distribution that describes the instant nodal temperature along the 700 μm in the y-axis (composed by the 15 data points/nodes) described in Fig. 13 for the DAM optimisation mechanism. The melting-solidification range shown in Fig. 14 is delimited by the solidus and liquidus temperatures of the powder (1385 and 1425 °C, respectively). The peak of the curve in Fig. 14 (i.e. maximum temperature) represents the melt-pool centre which is located at the plotted distance of 525 μm. It can be seen that the melt pool starts solidifying 150 μm behind the melt-pool centre in the scanning direction. The DAM s/d ratio along the scanning direction can be $s/d = 0.08$ (i.e. 0.15 mm solidification distance / 1.9 mm total multimode beam diameter). This will lead to significant reduction of the temperature gradient in DAM compared to SLM, which ultimately can result in reduced residual stress build-up.

Figure 15 shows the simulated temperature distribution and material solidification evolution of parts processed using the DAM optimisation mechanism in a range of views (plan, front and side cross-sections, and a dimensioned isometric view). Figure 15a shows the temperature distribution in the XY-plane (plan view) along the scanning direction. This takes the form of a uniform, non-elongated elliptical temperature distribution, which is expected from using a parallel multi-beam melting scheme and slow scanning velocities, and differs to the elongated-tail-shape temperature distribution with high-

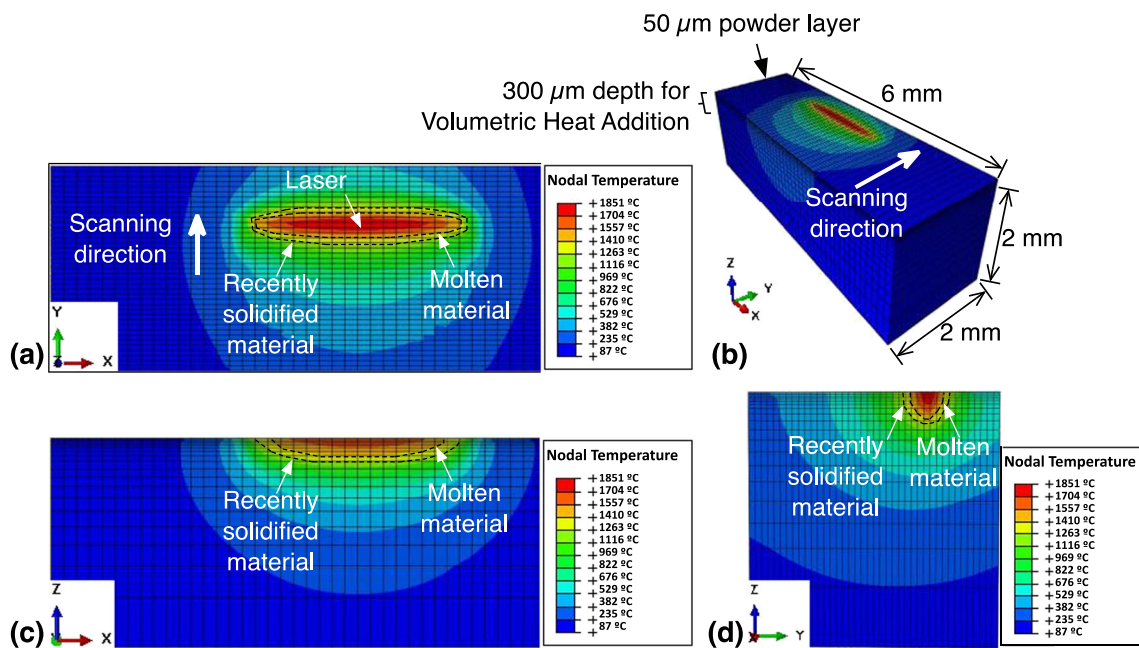


Fig. 15 **a** (Plan view) Simulated temperature and material solidification evolution along the scanning direction in XY-plane. **b** Dimensioned isometric view showing the depth used for volumetric heat addition. **c** (Front view) Temperature and material solidification evolution across the

depth of the scanning direction in XZ-plane. **d** (Side view) Temperature and material solidification evolution along the depth of the scanning direction in YZ-plane.

temperature gradients typical of SLM. The uniformity of the DAM temperature distribution reduces the temperature gradients along and across the scanning direction, resulting in lower heating and cooling rates. Figure 15b shows a dimensioned isometric view with scanning direction and the region used for volumetric heat addition. Figure 15c, d shows the temperature distribution in the XZ-plane (front view) and YZ-plane (side view) across and along the scanning direction, respectively. Uniform temperature distribution similar to that within the top surface can be observed in Figs. 15c, d, which might be evidence of uniform cooling rates and temperature gradients in all directions. The low-temperature gradient across and along the melt-pool depth in both the front and side view would lead to reduced contraction upon cooling, controlling the residual stress development as described by the temperature gradient mechanism and cool-down phase model presented in Sect. 1.2.

4.4 Cooling rate and temperature gradient

The correlation between temperature gradients and residual stress build-up in SLM has been previously described in Sect. 1.3. Low-temperature gradients inherent in the DAM process may also result in low residual stress build-up. In the DAM-optimised mechanism, the 100 μm scan intervals are composed by overlapping 100 μm laser spots, similar to the selective re-melting SLM mechanism described in Sect. 1.4 for hatch spacing = laser diameter. Figure 16a shows a typical SLM scanning strategy compared to that of DAM in Fig. 16b. The temperature evolution at the top surface of the powder bed in points A (similar to point A3 in Fig. 2a) and B for SLM

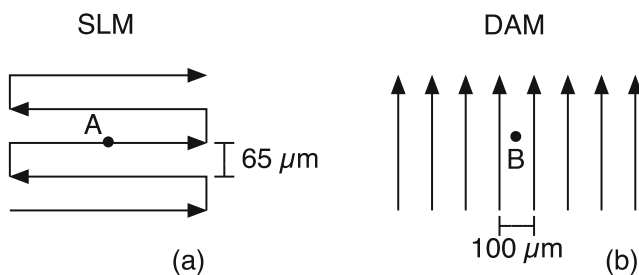


Fig. 16 **a** Typical SLM scanning strategy of a single raster scan vector. **b** DAM scanning strategy of parallel multi-scanning vectors (optimised)

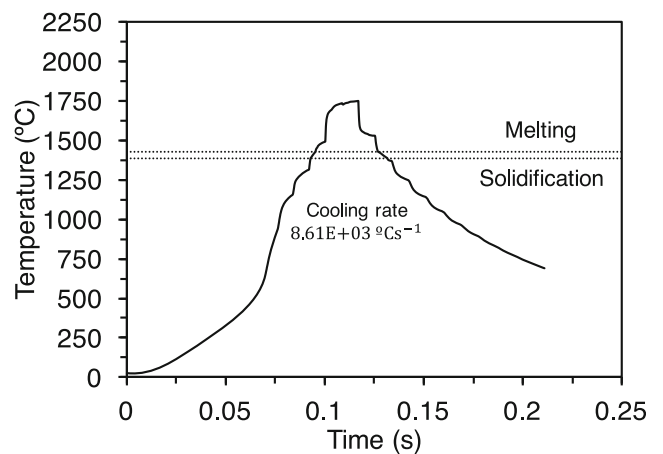
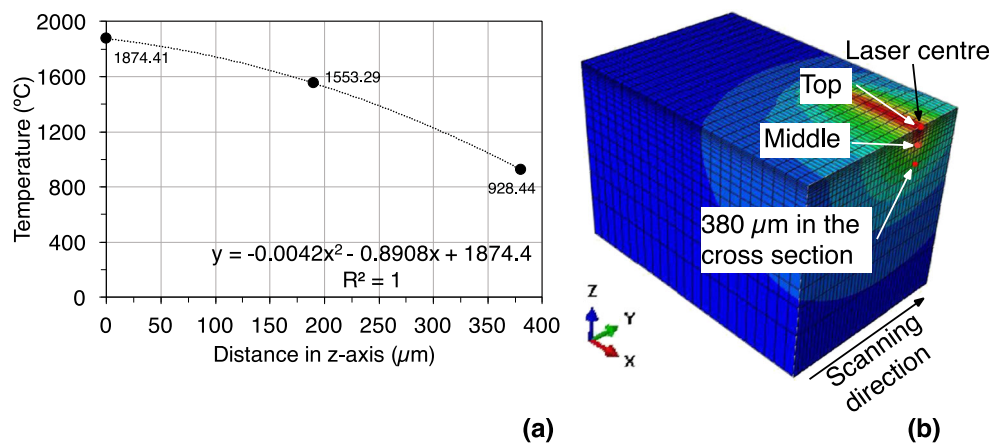


Fig. 17 Simulated DAM nodal thermal evolution of point B (in Fig. 16b) along the scanning direction

Fig. 18 **a** Temperature gradient prediction of the DAM optimised mechanism between the top surface of the melt, 190 and 380 μm below the melt-pool from FE simulation for DAM of 316L stainless steel one-layer components. **b** Cross-sectional view of the model showing the top, 190 and 380 μm position considered for temperature gradient estimation



and DAM, respectively, is compared in this section. Point A was selected since a stable melt depth and invariant cooling rate was observed as described in Sect. 1.3 and Fig. 2a. A similar behaviour was observed at point B in the DAM model. The scan interval (i.e. hatch distance in SLM) and distance between spots (i.e. spot period in DAM) for both SLM and DAM are 65 and 100 μm , respectively.

The thermal history of points A and B is analysed in order to compare their correspondent cooling rates. Point A is equivalent to point A3 in Fig. 2a in which thermal history is plotted in Fig. 2c. As mentioned before in Sect. 1.3, point A can be subjected to three peak melting temperatures with $2.08\text{E} + 05$, $1.07\text{E} + 05$ and $1.51\text{E} + 05$ $^\circ\text{C s}^{-1}$ cooling rate values, respectively. The simulated thermal history of point B (Fig. 16b) has been extracted from the optimised DAM model and is plotted in Fig. 17. Here, a DAM cooling rate $8.61\text{E} + 03$ $^\circ\text{C s}^{-1}$ can be calculated using Eq. 1, which can result in coarser microstructures than SLM, with $\lambda_1 = 4$, from Eq. 2. However, DAM cooling rates on the order of magnitude 10^3 are in the lower limit of typical values for rapid-solidification processing. Therefore, it is concluded that DAM can benefit from the superior mechanical properties that characterises rapid cooling mechanisms while exhibiting cooling rates low enough to avoid cracking.

Figure 18a shows the simulated depth-resolved temperature gradient for the DAM optimisation model, plotting the temperature at the top surface of the melt pool as well as 190 and 380 μm below the top surface of the melt-pool. These points are highlighted in the cross-section view of the model pictured in Fig. 18b. The equation shown in Fig. 18a describes the temperature distribution in the z-direction. It has been used for comparing the thermal distribution of DAM with that of SLM shown in Fig. 2d in the z-direction. A 132 μm penetration into substrate is predicted by the DAM model. Therefore, $\Delta z_{(\text{top surface to melt depth})}$ is $132 \mu\text{m} + 50 \mu\text{m}$ layer thickness = 182 μm . $\Delta T_{(\text{top surface to melt depth})}$ can be obtained using the equation in Fig. 18 to calculate temperature at a given z location (where $z = 0$ represents the top surface), which gives $|\Delta T / \Delta z|_{(\text{top surface to melt depth})} = 1.65$ $^\circ\text{C } \mu\text{m}^{-1}$ for DAM compared to the 11.16 $^\circ\text{C } \mu\text{m}^{-1}$ of SLM reported in Sect. 1.3. Therefore, the temperature gradients at the junction of the powder layer with the substrate (i.e. where the highest residual stresses are expected to develop) can be $11.16 / 1.65 = \sim 6.8$ times lower than SLM, which might result in a proportional reduction of residual stress formation. From Fig. 3, it can be assumed that the maximum levels of residual stresses ~ 350 MPa perpendicular and ~ 450 MPa parallel to the scanning direction of a one-layer part, typical in SLM of stainless steel, can be reduced to \sim

Fig. 19 Cross-view of the simulated substrate penetration depth using the DAM optimised model



50 and ~ 70 MPa, respectively, with ~ 6.8 lower temperature gradients, which can be characteristic of the DAM process.

4.5 Melt-pool penetration into substrate

Figure 19 shows a cross-sectional view of the simulated DAM penetration depth into substrate, using the optimised model.

The area in red represents the phase changes (i.e. powder-to-liquid-to-solid) of the laser-scanned layer of powder that was melted and solidified. The areas in blue represent the surrounding powder that was not scanned/melted by the laser. The simulated penetration depth of the DAM process is $132 \mu\text{m}$, which is comparable to that reported in literature for the same material. Higher melt depths in SLM are known to result from decreasing scanning velocities. Similarly, higher DAM penetration depths may be the result of the slower scanning speeds compared to SLM.

5 Conclusions

The computational efficiency of the adapted modelling approach for SLM simulation has proven to be applicable for DAM simulation using the appropriate boundary conditions. Melt-pool dimensions and thermal evolution with high correlation with published experimental results validated the modelling approach presented. The model was capable of predicting temperature evolution through the powder layer to the solid substrate, modelling the DAM limitation of inter-layer melt disruption reported in literature for processing multi-layer 316L stainless steel components. A DAM configuration with optimised energy density parameters has been modelled with $100 \mu\text{m}$ individual laser diameter, $100 \mu\text{m}$ spot period (i.e. hatch spacing), 100 W total laser power and 6.12 mm s^{-1} scan speed. The optimised energy density modelled has been compared with SLM for the same process material. It was observed that the DAM methodology can effectively reduce temperature gradient and cooling rates, theoretically reducing residual stress build-up due to its characteristic melting mechanism composed of multiple parallel scanning vectors with low individual power and low scan speeds. The analysis concludes that the predicted temperature gradients and cooling rates of DAM can match those of optimised pre-heated SLM mechanisms (either by selective re-melting, substrate pre-heating or both). It was observed that the melt-pool penetration depth in DAM of 316L stainless steel can be similar to values typical of SLM for the same process material. The present work analysed the thermal behaviour of a multi-beam array of low power lasers in additive manufacturing. The authors suggest that the DAM technique can significantly reduce temperature gradients and cooling rates of a laser-based additive manufacturing process, resulting in complete alleviation of residual stresses. The

thermal analysis described in the present work can be used to compare DAM with SLM in terms of mechanical behaviour, microstructure and residual stresses of as-built components in future work.

Acknowledgements The authors would like to acknowledge support from a UK Engineering & Physical Sciences Research Council (EP/K503812/1) IIKE Proof of Concept award and the Future Manufacturing Hub in Manufacture using Advanced Powder Processes (MAPP) (EP/P006566/1). Also acknowledge support from the Science and Technology National Council (CONACYT) of Mexico.

Open Access This article is distributed under the terms of the Creative Commons Attribution 4.0 International License (<http://creativecommons.org/licenses/by/4.0/>), which permits unrestricted use, distribution, and reproduction in any medium, provided you give appropriate credit to the original author(s) and the source, provide a link to the Creative Commons license, and indicate if changes were made.

Publisher's Note Springer Nature remains neutral with regard to jurisdictional claims in published maps and institutional affiliations.

References

- Zavala-Arredondo M, Boone N, Willmott J, Childs DTD, Ivanov P, Groom KM, Mumtaz K (2017) Laser diode area melting for high speed additive manufacturing of metallic components. *Mater Des* 117:305–315
- Zavala-Arredondo M, Groom KM, and Mumtaz K (2017) Diode area melting single-layer parametric analysis of 316L stainless steel powder. *Int J Adv Manuf Technol* 1–14
- Casavola C, Campanelli L, and Pappalettere C (2008) Experimental analysis of residual stresses in the selective laser melting process. in *Proceedings of the XIth International Congress and Exposition 3: 1479–1486*
- Withers PJ, Bhadeshia HKDH (2001) Residual stress. Part 2—nature and origins. *Mater Sci Technol* 17(4):366–375
- Mercelis P, Kruth J, Kruth J-P (2006) Residual stresses in selective laser sintering and selective laser melting. *Rapid Prototyp J* 12(3): 254–265
- Li L, Lough C, Replogle A, Bristow D, Landers R, and Kinzel E (2017) Thermal modeling of 304L stainless steel selective laser melting, in *Solid Freedom fabrication*, pp 1068–1081
- Ali H (2017) Evolution of residual stress in Ti6Al4V components fabricated using selective laser melting
- Smurov IY, Dubenskaya MA, Zhirnov IV, Teleshevskii VI (2016) Determination of the true temperature during selective laser melting of metal powders based on measurements with an infrared camera. *Meas Tech* 59(9):971–974
- Mills KC (2002) Recommended values of thermophysical properties for selected commercial alloys. Woodhead
- Yadroitsev I, Yadroitsava I (2015) Evaluation of residual stress in stainless steel 316L and Ti6Al4V samples produced by selective laser melting. *Virtual Phys Prototyp* 10(2):67–76
- Elmer JW, Allen SM, Eagar TW (1989) Microstructural development during solidification of stainless steel alloys. *Metall Trans A* 20(10):2117–2131
- Li R, Shi Y, Liu J, Yao H, Zhang W (2009) Effects of processing parameters on the temperature field of selective laser melting metal powder. *Powder Metall Met Ceram* 48(3–4):186–195

13. Kempen K, Vrancken B, Thijs L, Bols S, Van Humbeeck J, and Kruth J-P (2013) Lowering thermal gradients in Selective Laser melting by pre-heating the baseplate
14. Ali H, Ma L, Ghadbeigi H, Mumtaz K (2017) In-situ residual stress reduction, martensitic decomposition and mechanical properties enhancement through high temperature powder bed pre-heating of selective laser melted Ti6Al4V. *Mater Sci Eng A* 695:211–220
15. Kamath C, El-dasher B, Gallegos GF, King WE, Sisto A (2013) Density of additively-manufactured, 316L SS parts using laser powder-bed fusion at powers up to 400W. Lawrence Livermore National Laboratory, Livermore
16. Vaithilingam J, Goodridge RD, Hague RJM, Christie SDR, Edmondson S (2016) The effect of laser remelting on the surface chemistry of Ti6Al4V components fabricated by selective laser melting. *J Mater Process Technol* 232:1–8
17. Parry L, Ashcroft IA, Wildman RD (2016) Understanding the effect of laser scan strategy on residual stress in selective laser melting through thermo-mechanical simulation. *Addit Manuf* 12:1–15
18. Foroozmehr A, Badrossamay M, Foroozmehr E, Golabi I (2016) Finite element simulation of selective laser melting process considering optical penetration depth of laser in powder bed. *Mater Des* 89:255–263
19. Roberts IA (2012) Investigation of residual stresses in the laser melting of metal powders in additive layer manufacturing. University of Wolverhampton, Wolverhampton
20. Shi Y, Shen H, Yao Z, Hu J (2007) Temperature gradient mechanism in laser forming of thin plates. *Opt Laser Technol* 39:858–863
21. Zavala Arredondo MA (2017) Diode area melting use of high power diode lasers in additive manufacturing of metallic components. University of Sheffield, Sheffield